Reconstruction of wave function via spin-orbit interaction of light

Qiang Yang,[1] Dingyu Xu,[1] Shizhen Chen,[2] Shuangchun Wen,[2] and Hailu Luo[1,*]

[1] *Laboratory for Spin Photonics, School of Physics and Electronics, Hunan University, Changsha 410082, China*

[2] *Key Laboratory for Micro-/Nano-Optoelectronic Devices of Ministry of Education, School of Physics and Electronics, Hunan University, Changsha 410082, China*

(Received 29 June 2023; accepted 16 October 2023; published 6 November 2023)

The measurement of a wave function plays a pivotal role in quantum physics and presents a distinctive challenge in experiment. Recent works have shown that both the real and imaginary components of the wave function can be extracted by employing weak or strong measurements, thereby enabling the determination of its amplitude and phase. Here, we propose a simple approach for reconstructing the wave function utilizing the spin-orbit interaction of light at the air-glass interface. By directly measuring the amplitude and employing spatial differentiation to capture the phase gradient, it becomes possible to successfully reconstruct an unknown wave function. To demonstrate its feasibility, we experimentally measure the pure wave function of photons with a Gaussian state. Furthermore, we conduct measurements on a custom state featuring a targeted phase jump to examine the accuracy of our methodology. The measured results show a distribution with high contrast and considerable accuracy, with a fidelity that can exceed 85%. We believe that this work contributes valuable insights into the practical applications of spin-orbit interaction, including optical image processing, wave-front sensing, and quantitative phase imaging.

DOI: 10.1103/PhysRevApplied.20.054011

I. INTRODUCTION

The wave function, a complex-valued distribution, represents a quantum system and takes the center stage in quantum physics and quantum technology. The no-cloning theorem asserts that it is impossible to exactly reconstruct an arbitrary unknown quantum state [1–3]. The determination of an arbitrary wave function is therefore a challenging and important task. In performing a direct measurement on an ensemble of particles with the same wave function ψ, the result acquired is just the probability $|\psi|^2$ of finding a particle at a certain position or momentum. This is not enough to characterize the full wave function unambiguously. Instead, a conventional method, known as quantum state tomography [4–9], has been established to estimate the wave function through a large set of projective measurements. This strategy, however, still presents drawbacks in terms of simplicity, versatility, and directness.

Recently, Lundeen *et al*. [10] have proposed a more direct and simple measurement of the quantum wave function using weak measurement [11–13]. The use of "direct" means that the real and imaginary components of the wave function can be received directly on the measurement apparatus owing to the proportionality between the weak value and the wave function. Finally, the amplitude and phase of a pure quantum wave function can be obtained by performing specific calculations on the real and imaginary components. The method has subsequently been generalized to the measurement of mixed states [14–16], photon polarization [17], orbital angular momentum [18], and the Wigner distribution of twisted photons [19]. To date, several optimized schemes have been proposed in both direct [20,21] and indirect [22–26] methods, leveraging the principles of weak measurement. Furthermore, a recent noteworthy study argued that strong measurement with no approximation allows for better estimation of the quantum wave function [27]. In fact, the strong measurement scheme is also weak value based and has been raising significant interest [28–31]. In general, there are two feasible proposals to characterize the quantum state wave function: quantum state tomography and weak-value-based quantum measurement. The question of which method performs better has long been a point of contention [32–34].

In our scheme, we take advantage of the spin-orbit interaction of light at a simple air-glass interface to effectively reconstruct a pristine wave function. The spin-orbit interaction of light manifests itself as the mutual conversion and coupling between the spin and orbital angular momentum [35]. It occurs in many systems, such as the reflection or refraction of polarized beams at a planar interface [36–40], the focusing of light or scattering of small particles [41–43], and the propagation of paraxial beams in anisotropic media [44–48]. Specifically, in systems where

*hailuluo@hnu.edu.cn

the rotational symmetry is broken, the spin-orbit interaction gives rise to a type of geometric phase known as the spin-redirection Berry phase [49,50]. The gradient of this geometric phase in momentum space induces a spin-dependent beam splitting in real space, i.e., the spin Hall effect of light in reflection or refraction at the optical interface with the refractive-index gradient [36–39,51]. Recently, the utilization of this distinct phenomenon has led to the proposal and rapid adoption of spatial differentiation in diverse fields, encompassing optical-image edge detection [52,53], phase mining [54], and differential microscopy [55].

Here, we show that the spatial differentiation alters the probability distribution of the photons and that capturing the phase-gradient component makes it possible to reconstruct the initial wave function. Within this procedure, the phase gradients along the x and y directions are both required, so we introduce the spatial full differentiation when considering an arbitrary linearly polarized light beam impinging on the air-glass interface. We experimentally measure a pure wave function of photons with a Gaussian state and a customized state featuring a targeted phase jump to validate the feasibility and accuracy of our proposal.

II. THEORETICAL ANALYSIS OF RECONSTRUCTION OF WAVE FUNCTION

The spin-orbit interaction of light, arising from the reflection at an optical interface, can be attributed to the transverse nature of photonic polarization; i.e., the angular-spectrum components of the polarization experience distinct rotations to maintain transversality [36–38]. We consider an initial state $|\psi\rangle$ with the arbitrary linear-polarization state $|i\rangle = \cos\alpha\,|H\rangle + \sin\alpha\,|V\rangle$ reflecting from the air-glass interface, where α denotes the incident polarization angle, as schematically shown in Fig. 1(a). In the spin basis, this polarization state corresponds to

$$|i\rangle = \frac{1}{\sqrt{2}}\exp(-i\alpha)\,|+\rangle + \frac{1}{\sqrt{2}}\exp(i\alpha)\,|-\rangle\,. \qquad (1)$$

The unitary transformation operator of the coupling between the spin and the momentum of the photons reads as

$$\hat{U} = \exp[i\hat{\sigma}_3(\hat{k}_x\Delta x + \hat{k}_y\Delta y)]. \qquad (2)$$

Here, $\hat{k}_x$ and $\hat{k}_y$ represent the longitudinal and transverse momentum operators with $\hat{k}_x\,|\psi\rangle = k_x\,|\psi\rangle$ and $\hat{k}_y\,|\psi\rangle = k_y\,|\psi\rangle$, while $\hat{\sigma}_3 = |+\rangle\langle+| - |-\rangle\langle-|$ is the third Pauli operator that assigns eigenvalues $+1$ and -1 to $|+\rangle$ and $|-\rangle$, respectively. Consequently, the wave packets corresponding to the parallel and antiparallel spin states undergo shifts of Δx and Δy, respectively.

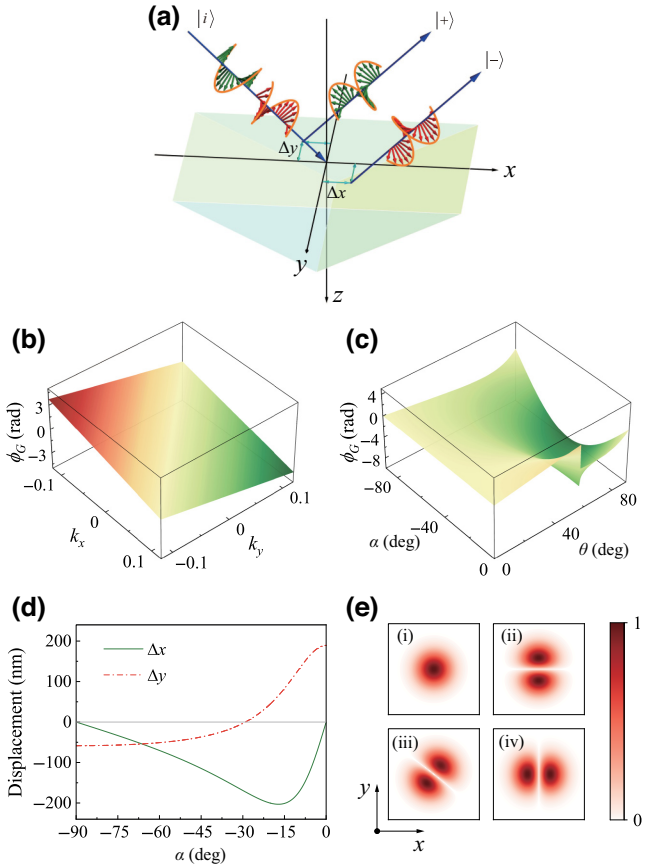

FIG. 1. The spin-orbit interaction of light at the air-glass interface. (a) A schematic diagram of the transverse and in-plane spin splitting when an arbitrary linearly polarized light beam impinges on the interface. (b) The geometric phase in momentum space. (c) The variation of the geometric phase with respect to the incident angle θ and an incident linear-polarization angle α. (d) The spin-dependent displacements Δx and Δy as a function of the incident linear-polarization angle α. (e) The probability amplitudes of the incident and reflected photons: (i) the probability amplitude $|\psi|^2$ for the incident Gaussian state; (ii)–(iv) the reflected probability amplitudes, which are proportional to $|\partial\psi/\partial y|^2$, $|\partial\psi/\partial x + \partial\psi/\partial y|^2$, and $|\partial\psi/\partial x|^2$, respectively.

While such spin splitting of a two-level system has been extensively examined within the context of weak measurement [51], here, we introduce an orthogonal and biased polarization analysis aimed at facilitating the occurrence of destructive interference between the two spin states to mine the phase of the wave function. After the interaction of incident photons with the optical interface, the beam state containing spin states at the air side of the interface can be written using $|\Psi\rangle = \hat{U}\,|\psi\rangle\,|i\rangle$ as (for more details, see Appendix A)

$$|\Psi\rangle = \frac{a}{\sqrt{2}}\exp(-i\alpha')\exp(i\phi_G)\,|\psi\rangle\,|+\rangle + \frac{a}{\sqrt{2}}\exp(i\alpha')\exp(-i\phi_G)\,|\psi\rangle\,|-\rangle\,, \qquad (3)$$

where the geometric phase $\phi_G = k_x\Delta x + k_y\Delta y$ and a derived parameter $a = \sqrt{(\cos\alpha r_p)^2 + (\sin\alpha r_s)^2}$, in which r_p and r_s are the Fresnel coefficients at the air-glass interface. During this evolution, the polarization angle rotates from α to $\alpha' = \arctan(r_s/r_p\tan\alpha)$. Note that in total internal reflection, $\alpha' = \alpha$ and $a = 1$. As is evident from a straightforward analysis, the spin-dependent displacement Δx and Δy can be readily determined by the gradient of the geometric phase ϕ_G in momentum space:

$$\begin{aligned}\Delta x &= \frac{\partial\phi_G}{\partial k_x} = \frac{r_p r_s\tan\alpha}{r_p^2 + r_s^2\tan^2\alpha}(\Delta_H - \Delta_V),\\ \Delta y &= \frac{\partial\phi_G}{\partial k_y} = \frac{r_p^2\delta_H + r_s^2\delta_V\tan^2\alpha}{r_p^2 + r_s^2\tan^2\alpha},\end{aligned} \tag{4}$$

where $\Delta_H = \partial\ln r_p/k_0\partial\theta$, $\Delta_V = \partial\ln r_s/k_0\partial\theta$, $\delta_H = (r_p + r_s)\cot\theta/k_0 r_p$, and $\delta_V = (r_p + r_s)\cot\theta/k_0 r_s$, with k_0 and θ being the wave number in vacuum and the incident angle, respectively.

Figure 1(b) displays the geometric phase in momentum space for a specific incident condition, while Fig. 1(c) illustrates the variation of the geometric phase of a particular photon with respect to the incident angle θ and the incident polarization angle α. To maintain the weak interaction in which the gradient of the geometric phase is small, we set $\theta = 45^\circ$ and select α to vary from -90° to 0°. The corresponding spin-dependent displacements Δx and Δy are shown in Fig. 1(d). If we choose the postselection state as

$$|f\rangle = \frac{1}{\sqrt{2}}\exp(-i\gamma)\,|+\rangle + \frac{1}{\sqrt{2}}\exp(i\gamma)\,|-\rangle\,, \tag{5}$$

where $\gamma = \alpha' + \pi/2$, to facilitate destructive interference between the two spin components, the final state $|\varphi\rangle = \langle f|\Psi\rangle$ evolves as

$$|\varphi\rangle = \frac{ia}{2}\left[\exp(i\phi_G)\,|\psi\rangle - \exp(-i\phi_G)\,|\psi\rangle\right]. \tag{6}$$

Under the action of Fourier transformation from the momentum space to the position space, the final wave function becomes

$$\varphi(x,y) = \frac{ia}{2}\left[\psi(x+\Delta x, y+\Delta y) - \psi(x-\Delta x, y-\Delta y)\right]. \tag{7}$$

For weak spin-orbit interaction of light, i.e., the spin-dependent displacements Δx and Δy are much smaller than the width of the incident wave packet, the final wave function $\varphi(x,y)$ is approximately proportional to the first-order spatial full differentiation of the initial wave function $\psi(x,y)$:

$$\varphi(x,y) \simeq ia\left[\Delta x\frac{\partial\psi(x,y)}{\partial x} + \Delta y\frac{\partial\psi(x,y)}{\partial y}\right]. \tag{8}$$

We then consider a Gaussian wave function at a given plane z_0,

$$\begin{aligned}\psi(x,y) = \frac{1}{w}\exp\left(-\frac{x^2+y^2}{w^2}\right)\\ \times\exp\left(ik_0 z_0 + ik_0\frac{x^2+y^2}{2R} - i\zeta\right),\end{aligned} \tag{9}$$

where $k_0 = 2\pi/\lambda$, $w = w_0\sqrt{1 + z_0^2/z_R^2}$ is the radius at the plane z_0 along the beam, w_0 is the waist radius, $R = z_0 + z_R^2/z_0$, $\zeta = \arctan(z_0/z_R)$, and $z_R = k_0 w_0^2/2$ is the Rayleigh length. The incident and reflected probability densities after differentiation are shown in Fig. 1(e). Focusing on this kind of spatial differentiation, one can achieve the purpose of optical image processing [56–59] and optical signal processing [60]. Nevertheless, here we aim to reconstruct a wave function. Note that for a given z_0, the phase $k_0 z_0$ and ζ are unambiguous. Hence, the phase that needs to be determined is only

$$\phi(x,y) = k_0\frac{x^2+y^2}{2R}. \tag{10}$$

For the sake of convenience, we express the wave function as $\psi(x,y) = A(x,y)\exp[i\phi(x,y)]$ with amplitude $A(x,y) = 1/w\exp\left[-(x^2+y^2)/w^2\right]$.

The amplitude, also known as the probability distribution, can be measured directly by the strong measurement. Regarding the phase, the application of spatial differentiation can transform it into the intensity distribution. However, this causes the amplitude and phase to become mixed in the differentiation of the wave function and appear in real and imaginary parts, respectively. To solve this problem, Zhu *et al.* have found that the information pertaining to the amplitude and phase can be inherently separated without the introduction of any additional auxiliary experimental setup [23]. Following this, we modify the postselection state in Eq. (5) by setting $\gamma = \alpha' + \beta + \pi/2$, in which the postselection angle β introduces a bias retardation. As a result, the final wave function in Eq. (8) evolves into

$$\begin{aligned}\varphi(x,y) \simeq -a\sin\beta\,\{\psi(x,y) - i\cot\beta\\ \times\left[\Delta x\frac{\partial\psi(x,y)}{\partial x} + \Delta y\frac{\partial\psi(x,y)}{\partial y}\right]\}.\end{aligned} \tag{11}$$

The probability density is defined as $P = |\varphi(x,y)|^2$. Expanding the differentiation of the wave function and designating the postselection angle as $\pm\beta$, the phase gradient

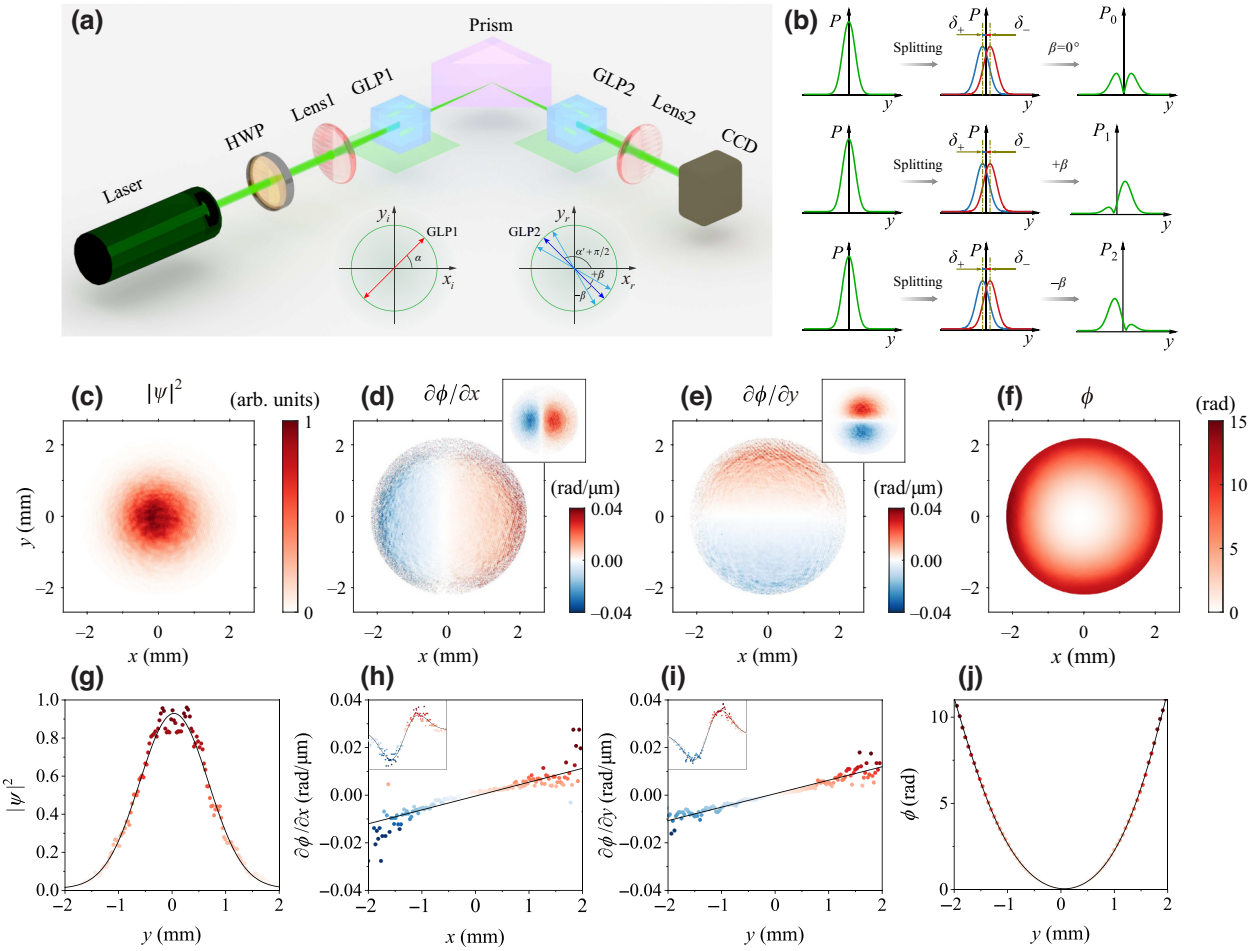

FIG. 2. The reconstruction of a pure wave function with a Gaussian state. (a) The experimental setup for the reconstruction of the wave function. The light source is a single-frequency visible laser at 532 nm (Coherent Verdi G5). Lenses 1 and 2 have effective focal lengths of 100 mm and 125 mm, respectively. HWP, half-wave plate (for adjusting the intensity); GLP1 and GLP2, Glan laser polarizers; CCD, charge-coupled device (Coherent LaserCam HR); "Prism," prism with refractive index $n = 1.515$ (BK7). The insets clarify GLP1 and GLP2, the axes of which are at angles α and $\alpha' + \pi/2 \pm \beta$ with x_i and x_r, respectively. (b) The evolution of the probability density as the postselection angle β changes after the spin-orbit interaction. (c) The directly measured amplitude $|\psi|^2$ of the Gaussian state. (d),(e) The measured phase gradients (d) $\partial\phi/\partial x$ and (e) $\partial\phi/\partial y$. The insets show the amplitude-dependent phase gradients $\kappa\Delta x A^2\partial\phi/\partial x$ and $\kappa\Delta y A^2\partial\phi/\partial y$, respectively. (f) The phase ϕ reconstructed from the phase gradients in (d) and (e). (g)–(j) A one-dimensional presentation of (c)–(f) with $x = 0$ in (c), (e), and (f) and $y = 0$ in (d). The inserts in (h) and (i) are also the one-dimensional presentations of the inserts in (d) and (e). The black solid lines are the corresponding best fits to the data.

can be calculated by the difference between two corresponding postselection probability density (for a detailed derivation, see Appendix C),

$$P_1 - P_2 = \kappa A^2(x,y)\left[\Delta x\frac{\partial\phi(x,y)}{\partial x} + \Delta y\frac{\partial\phi(x,y)}{\partial y}\right], \tag{12}$$

where $\kappa = 2a^2\sin 2\beta$. Thus, the phase gradient can be calculated through a direct inversion.

In order to reconstruct the phase, distinct measurements of the phase gradient are conducted along the x and y directions. We define $G_x = \partial\phi(x,y)/\partial x$ and $G_y = \partial\phi(x,y)/\partial y$ and write them in the vector form $G = (G_x\ G_y)^T$. The relation between the initial phase ϕ and the phase gradient G captured by each pixel on the optical detector is given as [61]

$$DG = d^{-1}E\phi, \tag{13}$$

where D and E are two sparse matrices related to pixels and d is the size of each pixel. Eventually, the phase ϕ can be retrieved by taking advantage of solving optimization problem $\min_{MN}\left|DG - d^{-1}E\phi\right|_2$, where MN is the number of pixels (for a detailed discussion of the phase reconstruction, see Appendix C).

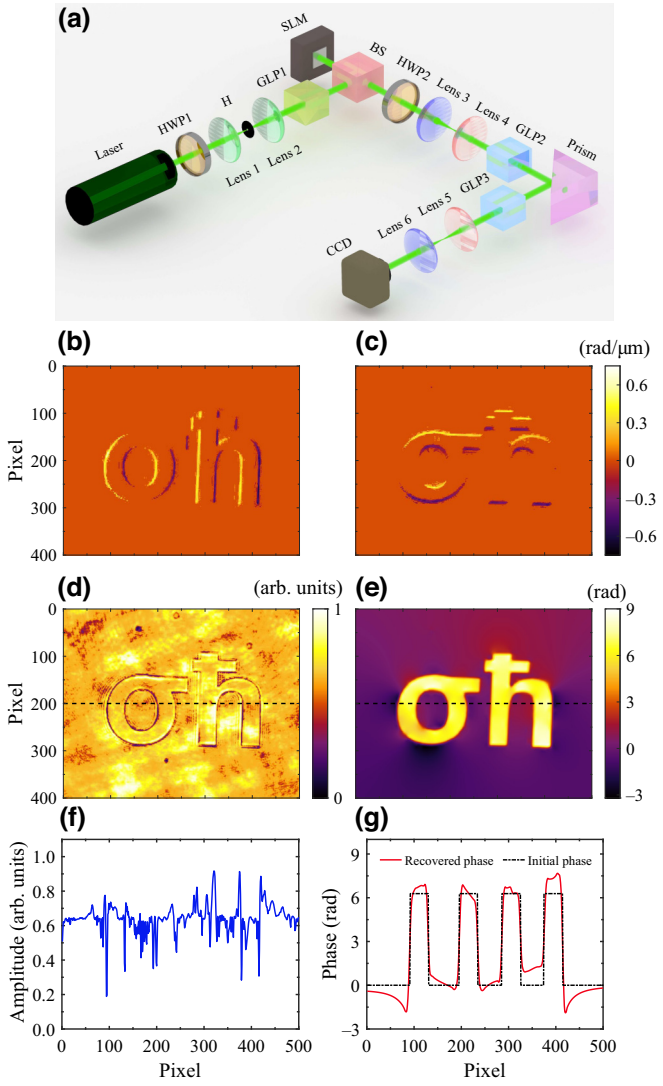

FIG. 3. A reconstruction of a custom state featuring a 2π phase jump with the spin angular momentum $\sigma\hbar$ distribution. (a) The experiment setup. SLM, spatial light modulator (for loading the phase distribution, Holoeye PLUTO-2.1-VIS); BS, 50:50 visible unpolarized beam splitter (Thorlabs BS013); GLP1 adjusts the polarization to be horizontal and HWP2 rotates the polarization to be vertical; lenses 1 and 2 form a confocal system; H, a pinhole with a diameter of 50 μm plugged in the confocal system to modulate the uniformity of the amplitude; lenses 3 and 6 form an imaging system. (b),(c) The phase gradients (b) $\partial\phi/\partial x$ and (c) $\partial\phi/\partial y$. (d),(e) The measured (d) amplitude and (e) reconstructed phase of the custom state. (f),(g) Cross sections along the black dashed lines in (d) and (e), respectively. (g) A comparison between the initial and the recovered phase.

III. EXPERIMENTAL RESULTS AND DISCUSSION

To demonstrate the feasibility of our protocol, we first experimentally measure a Gaussian wave function. The experiment setup is shown in Fig. 2(a). A Gaussian beam generated by a single-frequency visible laser at 532 nm passes through lens 1 and a polarizer (GLP1) to produce an initially polarized focused beam. Upon incidence of the beam onto the prism interface, the electric fields of the two spin components undergo distinct rotations to comply with the boundary condition. Consequently, the displacements of the two spin components, which are in opposite directions, are influenced by the input polarization state due to the polarization-dependent Fresnel reflections at the interface. The prism is affixed to a rotation stage, enabling meticulous manipulation of the incident angle θ. In our experiment, we set $\theta = 45°$. The incident polarization angle is selected by GLP1 with α. After reflection from the prism, the polarization angle is rotated to $\alpha' = \arctan(r_s/r_p \tan\alpha)$. Through the postselection of GPL2 with polarization angle $\gamma = \alpha' + \pi/2 \pm \beta$ and the collimation of lens 2, the final probability density of the photons is captured by a charge-coupled device (CCD). Figure 2(b) shows the evolution of the transverse probability density with the change of β. When $\beta = 0$, the two spin components interfere with each other and the probability distribution remains symmetrical, as explained in Eq. (8). On the other hand, when $\beta \neq 0$, destructive interference occurs, so that the symmetry of the distribution is broken, as indicated in Eq. (11).

The experiment results are illustrated in Figs. 2(c)–2(j). The probability amplitude $|\psi|^2$ shown in Fig. 2(c) is directly measured by setting $\gamma = \alpha'$. In the measurement, the incident polarization angle $\alpha = -90°$; thus there is no rotation of the polarization angle, i.e., $\alpha' = \alpha = -90°$. Therefore, the measured $|\psi|^2$ is indeed the probability amplitude of the initial wave function. The phase ϕ in Fig. 2(f) is reconstructed by the measured phase gradients, which are illustrated in Figs. 2(d) and 2(e), according to Eq. (13). It can be seen that the reconstructed phase is not perfectly symmetrical in the x direction, which is due to the asymmetry of the incident beam itself [Fig. 2(c)]. The two insets in Figs. 2(d) and 2(e) show the amplitude-dependent phase gradients $\kappa\Delta x A^2\partial\phi/\partial x$ and $\kappa\Delta y A^2\partial\phi/\partial y$, respectively. We set $\alpha = -29°$ ($\Delta y = 0$) and $-90°$ ($\Delta x = 0$) to obtain the phase gradients with respect to x and y, respectively, and the postselection angle $\beta = \pm 0.08°$. The one-dimensional experiment data and the corresponding best fits shown in Figs. 2(g)–2(j) verify excellent restructuring using our method. The photon count decreases at positions away from the center, resulting in more pronounced fluctuations in the phase gradient at those locations. Thus, reconstructing the wave function in more remote locations poses a significant challenge.

To further demonstrate the feasibility of our method, we use it to measure a custom state prepared using a phase mask depicting the spin angular momentum $\sigma\hbar$ with a phase jump of 2π. The phase mask is prepared via the spatial light modulator illuminated with the Gaussian beam from the laser. The experiment setup is shown in Fig. 3(a). Compared to the determination of the Gaussian

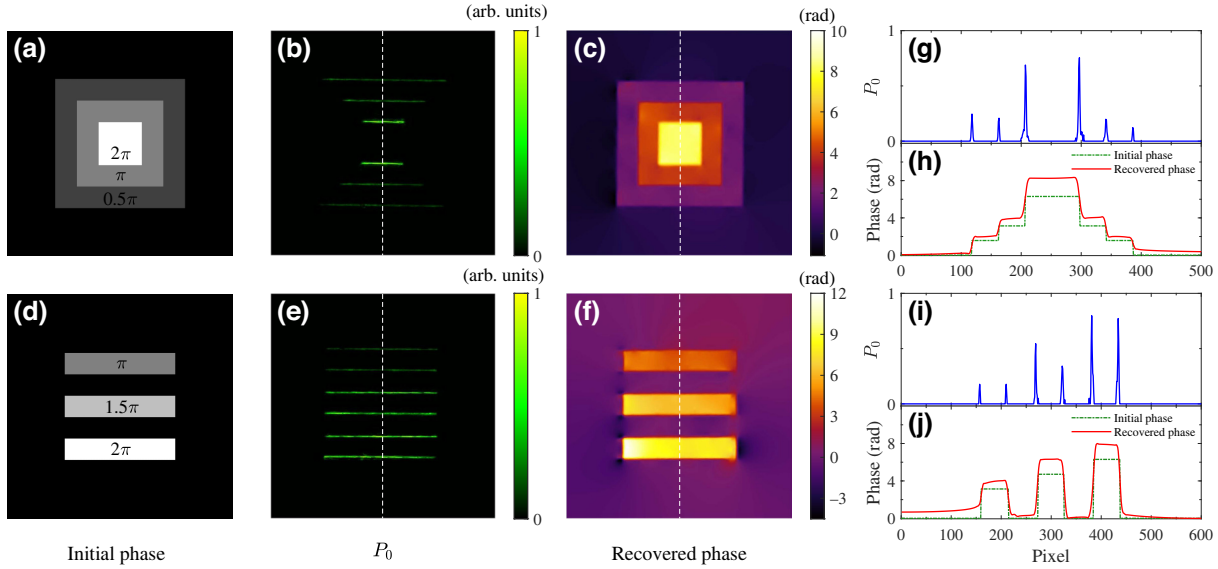

FIG. 4. Differential and quantitative phase imaging based on the spin-orbit interaction of light. (a),(d) The initial phase distributions of two custom states. The corresponding differential images and recovered phases are illustrated in (b) and (e), and (c) and (f), respectively. (g)–(j) Cross sections along the white dashed lines in (b), (c), (e), and (f). In (h) and (j), a comparison is made between the initial and the recovered phase.

wave function, we add two lenses (lenses 3 and 6) to image the phase mask. Generally, pure-phase objects are indistinguishable under direct illumination and the output state only experiences a phase change. We generate a Gaussian state the amplitude of which is approximately uniform to illuminate the phase mask. Then, the state that needs to be reconstructed is $\psi(x,y) = Ae^{i\phi(x,y)}$. To do this, one can use a telescope system, in which a pinhole is made in the confocal plane.

Despite the uniformity of the amplitude, the phase exhibits nonuniform characteristics [23]. In this case, the phase $\phi(x,y) = \phi_c(x,y) + \phi_g(x,y)$, where $\phi_c(x,y)$ and $\phi_g(x,y)$ represent the phase of the custom state and the Gaussian state, respectively. In fact, the magnitude of $\phi_g(x,y)$ is more than one order of magnitude smaller than that of $\phi_c(x,y)$, as shown in Figs. 2 and 3, so that $\phi_g(x,y)$ can be ignored, especially when the custom state is relatively small and located in the middle of the Gaussian state. However, upon introducing the postselection angle β, it is noteworthy that the phase gradient $\phi_g(x,y)$ may undergo amplification due to the inherent characteristics of our experimental apparatus as a weak measurement system, adhering to the principles of weak-value amplification [12,13]. To address this issue, we employ a method that utilizes bias to determine the sign of the phase gradient [54]. Taking Eq. (8) into account, the phase gradient with respect to x can be written as

$$G_x = \frac{\sqrt{P_0}}{a\Delta x A}\mathrm{sgn}(P_1 - P_2), \tag{14}$$

where P_0, P_1, and P_2 denote the probability density when we set the postselection angle as 0°, $+\beta^\circ$, and $-\beta^\circ$, respectively. Likewise, this also applies to G_y. In this way, the contribution of the Gaussian state to the phase gradient can be disregarded without amplification introduced by β, the appearance of which only determines the sign of the phase gradient. Unlike $G_x \propto \sqrt{P_0}\mathrm{sgn}(P_1 - P_0)$ (proposed in Ref. [54]), in which the bias to acquire P_1 needs to be very small, we provide a more flexible way in which P_1 and P_2 can be measured by setting any two symmetrical angles $\pm\beta$.

Figures 3(b) and 3(c) show two phase gradients along the x and y directions using Eq. (14). The amplitude and phase of the reconstructed state are shown in Figs. 3(d)–3(g). Note that the reconstructed phase distribution exhibits a high level of contrast. Figure 3(g) shows a comparison of the reconstructed phase and the initial phase. To provide a quantitative analysis of the accuracy, we calculate the fidelity between the recovered state $|\psi'\rangle$ and the initial state $|\psi\rangle$ as [20]

$$F(|\psi'\rangle, |\psi\rangle) = |\langle\psi'|\psi\rangle|. \tag{15}$$

The result is 70.08% for $M \times N = 200\,000$. Furthermore, the mean-square phase error that we calculate is 0.86. It should be emphasized that the determination of a state of such high dimensions (400×500) using state-by-state scanning is extremely time consuming [10,20,31]. However, our approach is scan free and opens up a practical route for the high-speed measurement of high-dimensional quantum systems. Furthermore, our method can be applied

to the differential and quantitative phase imaging of the biological cells and tissues.

To prove the hypothesis, we use two custom states with different phase steps and the corresponding differential and quantitative phase images are illustrated in Fig. 4. The differential images shown in Figs. 4(b) and 4(e) demonstrate that the magnitude of the phase value can be indicated by the intensity of the edge. Figures 4(g) and 4(i) give a clearer presentation. However, edge detection does not provide a more comprehensive representation of objects in imaging. Fortunately, we can accomplish the quantitative phase imaging by means of differential imaging, as shown in Figs. 4(c) and 4(f). The comparison between the recovered and the initial phase, as depicted in Figs. 4(h) and 4(j), substantiates the better accuracy of our method, albeit with an observable discrepancy. We also calculate the fidelity and the mean-square phase error between the recovered state and the initial state. In Fig. 4(c), the fidelity is 86.21% and the mean-square phase error is 0.29. In Fig. 4(f), the fidelity is 71.72% and the mean-square phase error is 0.79. We attribute the main sources of error to the following factors: first, variations in the beam displacement caused by the intricate optical path prior to observation; second, the presence of speckle and interference; and, lastly, potential inaccuracies in the calibration of the spatial light modulator, which can also result in the error between the reconstructed and prepared phase. In quantitative phase imaging, a precise measurement of the phase gradient holds significant importance in achieving enhanced accuracy.

IV. CONCLUSIONS

In summary, we have presented and validated a scan-free protocol for reconstructing the quantum wave function using the spin-orbit interaction of light. By directly measuring the amplitude and applying spatial differentiation to capture the phase, we have successfully reconstructed the pure wave function of Gaussian-state photons. Additionally, we have utilized a phase mask to prepare custom states, further demonstrating the feasibility and accuracy of our method. Our approach leverages the spin-orbit interaction of light at a fundamental optical interface, eliminating the need for complex experimental setups and procedures, thus offering the advantages of cost-effectiveness and simplicity. This work hopefully not only provides a deep comprehension of the physical implications of spin-orbit interaction but also enriches its applicability.

As an outlook, our method paves a way for the development of practical techniques with direct implications in the fields of wave-front sensing and quantitative phase imaging. Particularly in the regime of low photon levels, the development of quantum enhanced microscopy holds paramount importance in characterizing the microstructures and comprehending the dynamics of biological systems with a high signal-to-noise ratio and no photodamage [62,63]. Furthermore, although the measured wave function in our case is the spatial mode of photons, this scheme offers a conceptual framework to characterize the complex temporal wave function [64–66] with the help of temporal differentiation [67–69]. Moreover, we posit that the employment of spatial differentiation provides a viable approach to reconstruct the wave functions of other particles, such as neutrons and electrons. By introducing supplementary perturbations that influence the probability distribution of particles, the phase information of the wave function will likely be captured, although this may be beyond the reach of current technology.

ACKNOWLEDGMENTS

This work was supported by the National Natural Science Foundation of China (Grant No. 12174097) and the Natural Science Foundation of Hunan Province (Grant No. 2021JJ10008).

APPENDIX A: THE THEORY OF SPATIAL FULL DIFFERENTIATION

In this appendix, we provide a comprehensive derivation of the spatial full-differentiation theory based on the spin-orbit interaction of light. The transverse nature of photonic polarization is attributed to be the origin of the spin-orbit interaction of light upon reflection at an optical interface [36–38]. We begin with an incident wave packet polarized in the horizontal $|H\rangle$ or vertical $|V\rangle$ direction. Following reflection, the polarization states undergo evolution as [70]

$$\begin{aligned} |H(k_i)\rangle &\to r_p\left[|H(k_r)\rangle + k_{rx}\Delta_H\,|H(k_r)\rangle + k_{ry}\delta_H\,|V(k_r)\rangle\right], \\ |V(k_i)\rangle &\to r_s\left[|V(k_r)\rangle + k_{rx}\Delta_V\,|V(k_r)\rangle - k_{ry}\delta_V\,|H(k_r)\rangle\right], \end{aligned} \tag{A1}$$

where $r_{p,s}$ are the complex-valued reflection coefficients of the p and s waves, with $r_p = (n^2\cos\theta - \sqrt{n^2-\sin^2\theta})/(n^2\cos\theta + \sqrt{n^2-\sin^2\theta})$ and $r_s = (\cos\theta - \sqrt{n^2-\sin^2\theta})/(\cos\theta + \sqrt{n^2-\sin^2\theta})$, and

$$\begin{aligned} \Delta_H &= \frac{\partial \ln r_p}{k_0 \partial\theta}, \\ \Delta_V &= \frac{\partial \ln r_s}{k_0 \partial\theta}, \end{aligned} \tag{A2}$$

$$\begin{aligned} \delta_H &= \frac{(r_p + r_s)\cot\theta}{k_0 r_p}, \\ \delta_V &= \frac{(r_p + r_s)\cot\theta}{k_0 r_s}. \end{aligned} \tag{A3}$$

Here, k_0 is the wave number in vacuum, while n and θ denote the refractive index of glass and the incident

angle, respectively. Equations (A2) and (A3) represent the displacements of the Goos-Hänchen effect and the spin Hall effect, respectively, for the corresponding input polarization states.

In the spin space

$$\begin{aligned} |H\rangle &= \frac{1}{\sqrt{2}}(|+\rangle + |-\rangle), \\ |V\rangle &= \frac{i}{\sqrt{2}}(|-\rangle - |+\rangle), \end{aligned} \tag{A4}$$

the polarization state of the reflected field can be rewritten as

$$\begin{aligned} |H(k_i)\rangle \to{}& \frac{r_p}{\sqrt{2}}\left[\left(1 + k_{rx}\Delta_H - ik_{ry}\delta_H\right)|+\rangle \right. \\ &\left. + \left(1 + k_{rx}\Delta_H + ik_{ry}\delta_H\right)|-\rangle\right], \\ |V(k_i)\rangle \to{}& -\frac{ir_s}{\sqrt{2}}\left[\left(1 + k_{rx}\Delta_V - ik_{ry}\delta_V\right)|+\rangle \right. \\ &\left. - \left(1 + k_{rx}\Delta_V + ik_{ry}\delta_V\right)|-\rangle\right]. \end{aligned} \tag{A5}$$

For an arbitrary incident linear-polarization state,

$$|i\rangle = \cos\alpha\,|H\rangle + \sin\alpha\,|V\rangle\,, \tag{A6}$$

with the incident polarization angle α, the polarization state of reflected wave packet can be written as

$$\begin{aligned} |\varsigma\rangle \approx{}& \frac{1}{\sqrt{2}}\left(\cos\alpha r_p - i\sin\alpha r_s\right) \\ &\times \left(1 + ik_{rx}\Delta x + ik_{ry}\Delta y\right)|+\rangle \\ &+ \frac{1}{\sqrt{2}}\left(\cos\alpha r_p + i\sin\alpha r_s\right) \\ &\times \left(1 - ik_{rx}\Delta x - ik_{ry}\Delta y\right)|-\rangle\,, \end{aligned} \tag{A7}$$

where

$$\begin{aligned} \Delta x &= \frac{r_p r_s \tan\alpha}{r_p^2 + r_s^2\tan^2\alpha}(\Delta_H - \Delta_V), \\ \Delta y &= \frac{r_p^2\delta_H + r_s^2\delta_V\tan^2\alpha}{r_p^2 + r_s^2\tan^2\alpha}. \end{aligned} \tag{A8}$$

For the weak spin-orbit interaction of light, provided that the displacements Δx and Δy are much smaller than the beam-waist width w, the reflected field containing spin states $|\Psi\rangle = |\psi\rangle\,|\varsigma\rangle$ can be written as

$$\begin{aligned} |\Psi\rangle = {}& \frac{a}{\sqrt{2}}\exp(-i\alpha')\exp(ik_{rx}\Delta x + ik_{ry}\Delta y)\,|\psi\rangle\,|+\rangle \\ &+ \frac{a}{\sqrt{2}}\exp(i\alpha')\exp(-ik_{rx}\Delta x - ik_{ry}\Delta y)\,|\psi\rangle\,|-\rangle\,, \end{aligned} \tag{A9}$$

where $a = \sqrt{(\cos\alpha r_p)^2 + (\sin\alpha r_s)^2}$ and $\alpha' = \arctan(r_s/r_p\tan\alpha)$. Here, the approximations $\exp[\pm i(k_{rx}\Delta x + k_{ry}\Delta y)] \approx 1 \pm i(k_{rx}\Delta x + k_{ry}\Delta y)$ are introduced. Hence, we can define the evolution operator of the spin-orbit interaction as $\hat{U} = \exp\left[i\hat{\sigma}_3(\hat{k}_{rx}\Delta x + \hat{k}_{ry}\Delta y)\right]$, where $\hat{\sigma}_3 = |+\rangle\langle+| - |-\rangle\langle-|$ is the third Pauli operator that assigns eigenvalues $+1$ and -1 to $|+\rangle$ and $|-\rangle$, respectively. In Eq. (A9), we define the geometric phase $\phi_G = k_{rx}\Delta x + k_{ry}\Delta y$ such that parallel and antiparallel spin states occupy opposite geometric phases, resulting in translational motion along opposing directions.

Subsequently, we consider the reflected wave packet traversing a second polarizer, with the polarization axis denoted as $\gamma = \alpha' + \pi/2$, i.e., the postselection state reads as

$$|f\rangle = \cos\gamma\,|H\rangle + \sin\gamma\,|V\rangle\,. \tag{A10}$$

In the spin basis,

$$|f\rangle = \frac{1}{\sqrt{2}}\exp(-i\gamma)\,|+\rangle + \frac{1}{\sqrt{2}}\exp(i\gamma)\,|-\rangle\,. \tag{A11}$$

After destructive interference between the two spin components, the resultant wave function throughout the entire evolution can be determined by $|\varphi\rangle = \langle f\,|\Psi\rangle$ and the straightforward calculation yields

$$\begin{aligned} |\varphi\rangle &= \frac{a}{2}\exp[i(\gamma - \alpha')]\exp(ik_{rx}\Delta x + ik_{ry}\Delta y)\,|\psi\rangle \\ &\quad + \frac{a}{2}\exp[i(-\gamma + \alpha')]\exp(-ik_{rx}\Delta x - ik_{ry}\Delta y)\,|\psi\rangle \\ &= \frac{ia}{2}\exp(ik_{rx}\Delta x + ik_{ry}\Delta y)\,|\psi\rangle \\ &\quad - \frac{ia}{2}\exp(-ik_{rx}\Delta x - ik_{ry}\Delta y)\,|\psi\rangle\,. \end{aligned} \tag{A12}$$

By performing Fourier transformation on the angular spectrum of the reflected light field, we obtain the reflected wave function in position space:

$$\varphi(x,y) = \int\int \varphi(k_{rx},k_{ry})\exp\left[i(k_{rx}x + k_{rx}y)\right]dk_{rx}dk_{ry}. \tag{A13}$$

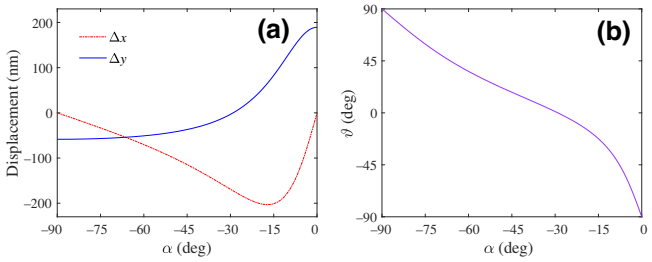

FIG. 5. The spin-dependent displacement (a) and the corresponding splitting direction angle ϑ (b) as a function of the incident polarization angle α for incident angle $\theta = 45°$.

Finally, the wave function can be obtained as

$$\varphi(x,y) = \frac{ia}{2}\left[\psi(x+\Delta x, y+\Delta y) - \psi(x-\Delta x, y-\Delta y)\right]. \tag{A14}$$

For weak spin-orbit interaction of light—i.e., when the spin-dependent displacement Δx and Δy are much smaller than the width of incident wave packet—the final wave function $\varphi(x,y)$ is approximately proportional to the first-order spatial full differentiation of the initial wave function $\psi(x,y)$:

$$\varphi(x,y) \simeq ia\left[\Delta x\frac{\partial\psi(x,y)}{\partial x} + \Delta y\frac{\partial\psi(x,y)}{\partial y}\right]. \tag{A15}$$

APPENDIX B: DIFFERENTIAL AND BIASED IMAGING

Referring to Appendix A, as shown in Eq. (A15), the final wave function $\varphi(x,y)$ is approximately proportional to the differentiation of the initial wave function $\psi(x,y)$. For imaging, including intensity and phase objects, the camera captures the edge information, thereby performing differential imaging. We can vary the incident polarization angle α to determine the corresponding spin-dependent displacement. We define the splitting direction angle as

$$\vartheta = \arctan\left(\frac{\Delta y}{\Delta x}\right). \tag{B1}$$

Then, the different displacements Δx and Δy can realize differential imaging in different directions. The theoretical predictions and experimental results are illustrated in Figs. 5 and 6, respectively.

When we take the bias into account, i.e., the polarization axis of the second polarizer is $\gamma = \alpha' + \beta + \pi/2$, where β is the postselection angle, the resulting evolution of the final wave function in Eq. (A15) can be changed as

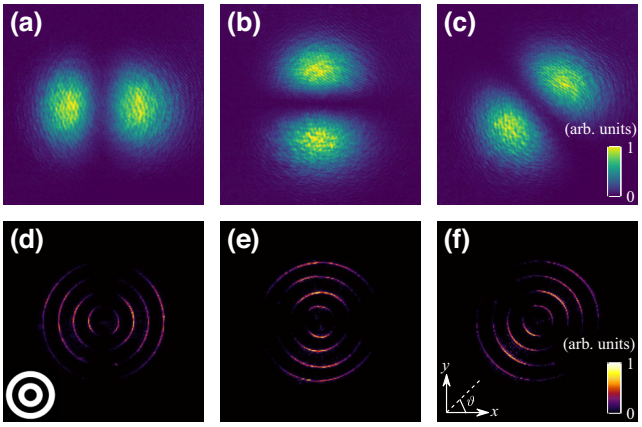

FIG. 6. The spatial differentiation of the Gaussian wave function and the corresponding differential imaging of the custom phase object. The incident polarization angles α are set to (a) $-29°$, (b) $-90°$, and (c) $-66°$. Then, the corresponding splitting direction angles ϑ are (d) 0°, (e) 90°, and (f) 45°, respectively. The inset in (d) shows the phase distribution of the custom state.

follows:

$$\varphi(x,y) \simeq -a\sin\beta\left[\psi(x,y) - i\cot\beta\Delta x\frac{\partial\psi(x,y)}{\partial x} - i\cot\beta\Delta y\frac{\partial\psi(x,y)}{\partial y}\right]. \tag{B2}$$

In this case, biased imaging can be achieved. We theoretically simulate and experimentally demonstrate the feasibility of biased imaging, as shown in Fig. 7. This tunable differential and biased imaging provides different contrasts and perspectives for observing phase objects. Additionally, it plays a key auxiliary role in quantitative phase imaging.

APPENDIX C: THE PHASE-GRADIENT CALCULATION AND PHASE RECONSTRUCTION

To reconstruct the phase distribution, it is very important to obtain the phase gradient from the differential operation. Considering a wave function $\psi(x,y) = A(x,y)e^{i\phi(x,y)}$ and substituting it into Eq. (B2) yields

$$\varphi(x,y) \simeq -a\sin\beta\left\{\psi(x,y) - i\cot\beta\times\left[\Delta x\frac{\partial\ln A(x,y)}{\partial x} + \Delta y\frac{\partial\ln A(x,y)}{\partial y}\right]\psi(x,y) + \cot\beta\left[\Delta x\frac{\partial\phi(x,y)}{\partial x} + \Delta y\frac{\partial\phi(x,y)}{\partial y}\right]\psi(x,y)\right\}. \tag{C1}$$

The probability density is defined as $P = |\varphi(x,y)|^2$. By rotating the postselection angle to $\pm\beta$ and denoting the corresponding detection probability intensity as P_1 and P_2,

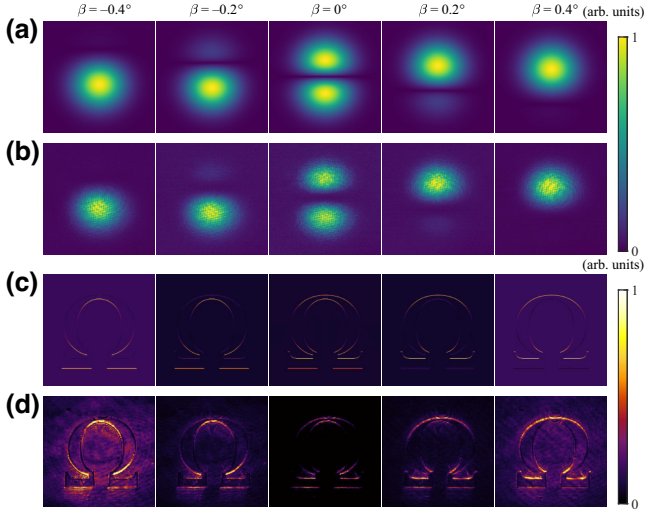

FIG. 7. The differential and biased imaging of the Gaussian wave function and the phase object. (a),(b) The differentiation and bias of the Gaussian wave function in (a) theory and (b) experiment, respectively. (c),(d) The (c) simulated and (d) experimental results of differential and biased imaging for a phase object depicting the letter Ω. We set the postselection angles to $\beta = -0.4^\circ, -0.2^\circ, 0^\circ, 0.2^\circ$, and 0.4°, respectively. The presented biased imaging occurs in the y direction, achieved by setting the incident polarization angle $\alpha = -90^\circ$. By altering the pre- and postselection states as well as adjusting the postselection angle β, one can achieve biased imaging with an adjustable contrast in any desired direction.

the differentiation of the phase part can be separated as follows:

$$P_1 - P_2 = \kappa A^2(x,y)\left[\Delta x\frac{\partial\phi(x,y)}{\partial x} + \Delta y\frac{\partial\phi(x,y)}{\partial y}\right], \tag{C2}$$

where $\kappa = 2a^2 \sin 2\beta$.

As an another example, if we consider a custom state $\psi(x,y) = Ae^{i\phi(x,y)}$ and substitute it into Eq. (A15), the probability density reads

$$P_0 = \left|aA\left[\Delta x\frac{\partial\phi(x,y)}{\partial x} + \Delta y\frac{\partial\phi(x,y)}{\partial y}\right]\right|^2. \tag{C3}$$

In addition, Zhu *et al.* have found that the bias introduced by β can determine the sign of the phase gradient [54]. Inspired by this, the phase gradients $G_x = \partial\phi(x,y)/\partial x$ and $G_y = \partial\phi(x,y)/\partial y$ can be obtained as

$$G_x = \frac{\sqrt{P_0^x}}{a\Delta xA}\mathrm{sgn}(P_1^x - P_2^x),$$
$$G_y = \frac{\sqrt{P_0^y}}{a\Delta yA}\mathrm{sgn}(P_1^y - P_2^y). \tag{C4}$$

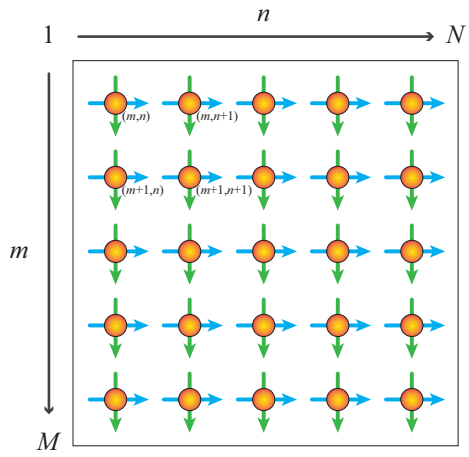

FIG. 8. The sampling geometry for measuring slopes and mesh points for the wave front. The arrows represent the position and direction of the sampling slope and the spheres represent the phase point that needs to be reconstructed.

This measurement of the phase gradient can also be called the slope measurement.

We write the phase gradient in the vector form $G = (G_x\ G_y)^T$ and discuss the phase-reconstruction process in detail. We consider the grid geometry proposed by Southwell [61], as shown in Fig. 8. The arrows indicate the slope directions of each point. The phase gradient between adjacent points in each direction is equal to the average of the measured slopes between those adjacent points, which leads to the correlation

$$\frac{(G^x_{m,n+1} + G^x_{m,n})}{2} = \frac{(\phi_{m,n+1} - \phi_{m,n})}{d}, \quad \begin{cases} m = 1, M, \\ n = 1, N-1, \end{cases}$$
$$\frac{(G^y_{m+1,n} + G^y_{m,n})}{2} = \frac{(\phi_{m+1,n} - \phi_{m,n})}{d}, \quad \begin{cases} m = 1, M-1, \\ n = 1, N. \end{cases} \tag{C5}$$

This equation can be written in the matrix form

$$DG = d^{-1}E\phi, \tag{C6}$$

where D and E are two sparse matrices and d is the size of each pixel. Besides, D and E are determined based on the size of M and N. The elements of matrix D are 0 and 0.5, while the elements of matrix E are 0, 1, and -1. To recover the phase ϕ, it is straightforward to apply the least-squares method. The corresponding normal equation reads

$$E^\dagger E\phi = dE^\dagger DG. \tag{C7}$$

In the case of large arrays, one can exploit the sparsity of matrix $E^\dagger E$ and employ iterative matrix methods to solve Eq. (C7), (for more details, see Ref. [61]). Figure 9 shows

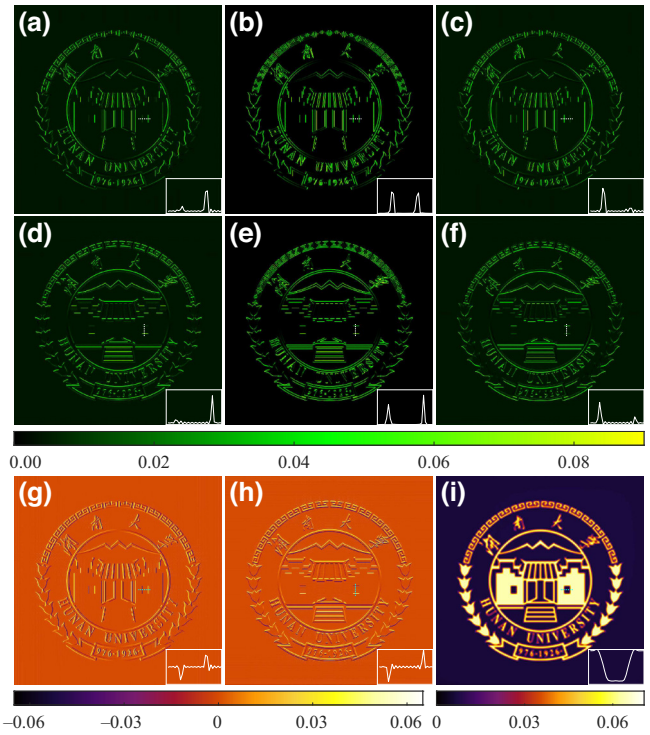

FIG. 9. A simulated calculation of the phase-gradient and phase-retrieval procedure of a phase target. (a)–(f) Six biased images with postselection angles of 0.15°, 0°, and −0.15° in the x and y directions, respectively: (a) P_1^x (0.15°); (b) P_0^x (0°); (c) P_2^x (−0.15°); (d) P_1^y (0.15°); (e) P_0^y (0°); (f) P_2^y (−0.15°). (g),(h) The calculated phase gradients with respect to x and y according to (a)–(f) by means of Eq. (C4): (g) G_x; (h) G_y. (i) The phase ϕ reconstructed by the phase gradients in (g) and (h). The insets represent the cross sections of the corresponding dashed lines to clearly give the distinction between different images.

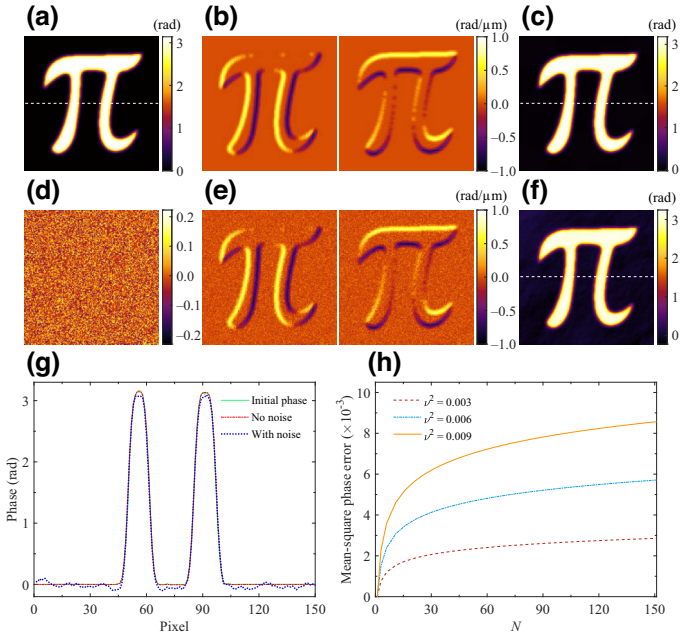

FIG. 10. Noise and error analysis in the reconstruction algorithm. (a) The initial phase distribution with a phase jump of π. (b) The phase gradients in the x and y directions. (c) The phase reconstructed from (b). (d) The random noise added in (b) with a variance of 0.003. (e),(f) The phase gradients (e) and the reconstructed phase (f) in the presence of noise. (g) Cross sections along the white dashed lines in (a), (c), and (f). (h) The mean-square phase error expressed by Eq. (C13).

the simulated calculation of the phase-gradient and the phase-retrieval procedure of a pure-phase object.

In the reconstruction process, there are two main sources of error. One is the algorithm accuracy, which depends on the shape of the wave front to be reconstructed. It is effective to reconstruct the wave front with any tilts, defocus, and astigmatism, regardless of the size $M(N)$. However, the model is imperfect when dealing with a wave front containing higher-order aberrations and the degree of error depends on the value of $M(N)$. This error arises primarily due to the finite sampling density.

The other source of error originates from the noise in the calculation of the phase gradient. We first simulate the error from the noise in the slope measurement. Before this, we analyze the reconstruction error without introducing additional noise, as shown in Figs. 10(a)–10(c). In this case, the mean-square error for the phase between the reconstructed result and the initial phase is 0.0022. We then assume that our measurement of the phase gradient contains random additive noise ν. Figures 10(d)–10(f) give the results in the presence of noise with a variance of 0.003. The calculated mean-square error between the reconstructed and the initial phase is 0.0054.

To give a specific expression, we write

$$G = G_0 \pm \nu, \tag{C8}$$

and consider the resulting phase error ϵ, i.e.,

$$\phi = \phi_0 \pm \epsilon. \tag{C9}$$

Applying the linear relationship of Eq. (C7), we have

$$E^\dagger E(\phi_0 \pm \epsilon) = E^\dagger D(G_0 \pm \nu). \tag{C10}$$

Here, we set $d = 1$. Hence, the phase error ϵ obeys the same normal equation as the phase itself, i.e.,

$$\epsilon = B\nu, \tag{C11}$$

where $B = (E^\dagger E)^{-1}E^\dagger D$. One of the phase-error components is $\epsilon_m = \sum_i B_{m,i}\nu_i$. Taking the statistical average of

$\epsilon_m \epsilon_n$ yields

$$\langle \epsilon_m \, \epsilon_n \rangle = \sum_i \sum_j B_{m,i} \, B_{n,j} \, \langle \nu_i \, \nu_j \rangle. \tag{C12}$$

Here, $\langle \nu_i \, \nu_j \rangle = \nu^2 \delta_{i,j}$ because of the independence of ν_i and ν_j. Then, Eq. (C12) simplifies to $\langle \epsilon_m \, \epsilon_n \rangle = \nu^2 \sum_i B_{m,i} \, B_{n,i}$. If $M = N$ (i.e., $m = n$), the mean-square phase error ε becomes

$$\varepsilon = \frac{1}{N^2} \sum_m \langle \epsilon_m^2 \rangle = \frac{\nu^2}{N^2} \sum_m \sum_i B_{m,i}^2. \tag{C13}$$

This shows that for a given N, the mean-square phase error ε is proportional to the variance ν^2 of the measurement noise. Figure 10(h) displays the mean-square phase error ε as a function of N under the conditions of three different variances, $\nu^2 = 0.003$, 0.006, and 0.009. When $\nu^2 = 0.003$ and $N = 150$, our simulated mean-square phase error $\varepsilon = 0.0054 - 0.0022 = 0.0032$ is close to the theoretical result, $\varepsilon = 0.0029$.

In our experiment, the main error is caused by the noise and especially the inaccuracy of the measured phase gradient, because the technical noise in the reconstruction itself is tiny. In addition, compared with experimental noise, the deviation of the phase-gradient value greatly affects the phase error (see Figs. 3 and 4). From Eq. (C4), we can see that the phase gradient mainly depends on the measurement of P_0^x (P_0^y) and A and the determination of the spin-dependent displacement $\Delta x, y$. For the measurement of P_0^x (P_0^y) and A, the slight interference of the light field can introduce the error. In addition, there is a deviation in the spin-dependent displacement Δx (Δy) on the CCD plane compared to the initial interface, despite accounting for modulation by the lens during imaging. It is worth mentioning that the condition for the establishment of differential operation is a small enough displacement, so the value of Δx (Δy) is also a factor that affects the measurement accuracy. Addressing the aforementioned issues can yield more precise reconstruction outcomes.

[1] W. K. Wootters and W. H. Zurek, A single quantum cannot be cloned, Nature **299**, 802 (1982).

[2] D. Dieks, Communication by EPR devices, Phys. Lett. A **92**, 271 (1982).

[3] P. W. Milonni and M. L. Hardies, Photons cannot always be replicated, Phys. Lett. A **92**, 321 (1982).

[4] K. Vogel and H. Risken, Determination of quasiprobability distributions in terms of probability distributions for the rotated quadrature phase, Phys. Rev. A **40**, 2847 (1989).

[5] D. T. Smithey, M. Beck, M. G. Raymer, and A. Faridani, Measurement of the Wigner distribution and the density matrix of a light mode using optical homodyne tomography: Application to squeezed states and the vacuum, Phys. Rev. Lett. **70**, 1244 (1993).

[6] G. Breitenbach, S. Schiller, and J. Mlynek, Measurement of the quantum states of squeezed light, Nature **387**, 471 (1997).

[7] A. G. White, D. F. V. James, P. H. Eberhard, and P. G. Kwiat, Nonmaximally entangled states: Production, characterization, and utilization, Phys. Rev. Lett. **83**, 3103 (1999).

[8] D. F. V. James, P. G. Kwiat, W. J. Munro, and A. G. White, Measurement of qubits, Phys. Rev. A **64**, 052312 (2001).

[9] M. Hofheinz, H. Wang, M. Ansmann, R. C. Bialczak, E. Lucero, M. Neeley, A. D. O'Connell, D. Sank, J. Wenner, J. M. Martinis, and A. N. Cleland, Synthesizing arbitrary quantum states in a superconducting resonator, Nature **459**, 546 (2009).

[10] J. S. Lundeen, B. Sutherland, A. Patel, C. Stewart, and C. Bamber, Direct measurement of the quantum wavefunction, Nature **474**, 188 (2011).

[11] Y. Aharonov, D. Z. Albert, and L. Vaidman, How the result of a measurement of a component of the spin of a spin-1/2 particle can turn out to be 100, Phys. Rev. Lett. **60**, 1351 (1988).

[12] J. Dressel, M. Malik, F. M. Miatto, A. N. Jordan, and R. W. Boyd, Colloquium: Understanding quantum weak values: Basics and applications, Rev. Mod. Phys. **86**, 307 (2014).

[13] A. N. Jordan, J. Martínez-Rincón, and J. C. Howell, Technical advantages for weak-value amplification: When less is more, Phys. Rev. X **4**, 011031 (2014).

[14] J. S. Lundeen and C. Bamber, Procedure for direct measurement of general quantum states using weak measurement, Phys. Rev. Lett. **108**, 070402 (2012).

[15] G. S. Thekkadath, L. Giner, Y. Chalich, M. J. Horton, J. Banker, and J. S. Lundeen, Direct measurement of the density matrix of a quantum system, Phys. Rev. Lett. **117**, 120401 (2016).

[16] Y. Zhou, J. Zhao, D. Hay, K. McGonagle, R. W. Boyd, and Z. Shi, Direct tomography of high-dimensional density matrices for general quantum states of photons, Phys. Rev. Lett. **127**, 040402 (2021).

[17] J. Z. Salvail, M. Agnew, A. S. Johnson, E. Bolduc, J. Leach, and R. W. Boyd, Full characterization of polarization states of light via direct measurement, Nat. Photonics **7**, 316 (2013).

[18] M. Malik, M. Mirhosseini, M. P. Lavery, J. Leach, M. J. Padgett, and R. W. Boyd, Direct measurement of a 27-dimensional orbital-angular-momentum state vector, Nat. Commun. **5**, 3115 (2014).

[19] M. Mirhosseini, O. S. Magaña-Loaiza, C. Chen, S. M. Hashemi Rafsanjani, and R. W. Boyd, Wigner distribution of twisted photons, Phys. Rev. Lett. **116**, 130402 (2016).

[20] M. Mirhosseini, O. S. Magaña-Loaiza, S. M. Hashemi Rafsanjani, and R. W. Boyd, Compressive direct measurement of the quantum wave function, Phys. Rev. Lett. **113**, 090402 (2014).

[21] Z. Shi, M. Mirhosseini, J. Margiewicz, M. Malik, F. Rivera, Z. Zhu, and R. W. Boyd, Scan-free direct measurement of an extremely high-dimensional photonic state, Optica **2**, 388 (2015).

[22] M. Yang, Y. Xiao, Y.-W. Liao, Z.-H. Liu, X.-Y. Xu, J.-S. Xu, C.-F. Li, and G.-C. Guo, Zonal reconstruction of photonic wavefunction via momentum weak measurement, Laser Photon. Rev. **14**, 1900251 (2020).

[23] J. Zhu, A. Wang, X. Liu, Y. Liu, Z. Zhang, and F. Gao, Reconstructing the wave function through the momentum weak value, Phys. Rev. A **104**, 032221 (2021).
[24] Y. Zheng, M. Yang, Z.-H. Liu, J.-S. Xu, C.-F. Li, and G.-C. Guo, Detecting momentum weak value: Shack-Hartmann versus a weak measurement wavefront sensor, Opt. Lett. **46**, 5352 (2021).
[25] Y. Zheng, M. Yang, Z.-H. Liu, J.-S. Xu, C.-F. Li, and G.-C. Guo, Toward practical weak measurement wavefront sensing: Spatial resolution and achromatism, Opt. Lett. **47**, 2734 (2022).
[26] Y. Zheng, M. Yang, Y.-W. Liao, J.-S. Xu, C.-F. Li, and G.-C. Guo, Reconstructing the multiphoton spatial wave function with coincidence wave-front sensing, Phys. Rev. A **107**, 042608 (2023).
[27] G. Vallone and D. Dequal, Strong measurements give a better direct measurement of the quantum wave function, Phys. Rev. Lett. **116**, 040502 (2016).
[28] P. Zou, Z.-M. Zhang, and W. Song, Direct measurement of general quantum states using strong measurement, Phys. Rev. A **91**, 052109 (2015).
[29] T. Denkmayr, H. Geppert, H. Lemmel, M. Waegell, J. Dressel, Y. Hasegawa, and S. Sponar, Experimental demonstration of direct path state characterization by strongly measuring weak values in a matter-wave interferometer, Phys. Rev. Lett. **118**, 010402 (2017).
[30] L. Calderaro, G. Foletto, D. Dequal, P. Villoresi, and G. Vallone, Direct reconstruction of the quantum density matrix by strong measurements, Phys. Rev. Lett. **121**, 230501 (2018).
[31] C.-R. Zhang, M.-J. Hu, Z.-B. Hou, J.-F. Tang, J. Zhu, G.-Y. Xiang, C.-F. Li, G.-C. Guo, and Y.-S. Zhang, Direct measurement of the two-dimensional spatial quantum wave function via strong measurements, Phys. Rev. A **101**, 012119 (2020).
[32] E. Haapasalo, P. Lahti, and J. Schultz, Weak versus approximate values in quantum state determination, Phys. Rev. A **84**, 052107 (2011).
[33] L. Maccone and C. C. Rusconi, State estimation: A comparison between direct state measurement and tomography, Phys. Rev. A **89**, 022122 (2014).
[34] D. Das and Arvind, Estimation of quantum states by weak and projective measurements, Phys. Rev. A **89**, 062121 (2014).
[35] K. Y. Bliokh, F. J. Rodríguez-Fortuño, F. Nori, and A. V. Zayats, Spin-orbit interactions of light, Nat. Photonics **9**, 796 (2015).
[36] M. Onoda, S. Murakami, and N. Nagaosa, Hall effect of light, Phys. Rev. Lett. **93**, 083901 (2004).
[37] O. Hosten and P. Kwiat, Observation of the spin Hall effect of light via weak measurements, Science **319**, 787 (2008).
[38] K. Y. Bliokh and Y. P. Bliokh, Conservation of angular momentum, transverse shift, and spin Hall effect in reflection and refraction of an electromagnetic wave packet, Phys. Rev. Lett. **96**, 073903 (2006).
[39] H. Luo, X. Zhou, W. Shu, S. Wen, and D. Fan, Enhanced and switchable spin Hall effect of light near the Brewster angle on reflection, Phys. Rev. A **84**, 043806 (2011).
[40] A. Aiello, N. Lindlein, C. Marquardt, and G. Leuchs, Transverse angular momentum and geometric spin Hall effect of light, Phys. Rev. Lett. **103**, 100401 (2009).
[41] O. G. Rodríguez-Herrera, D. Lara, K. Y. Bliokh, E. A. Ostrovskaya, and C. Dainty, Optical nanoprobing via spin-orbit interaction of light, Phys. Rev. Lett. **104**, 253601 (2010).
[42] M. Neugebauer, J. S. Eismann, T. Bauer, and P. Banzer, Magnetic and electric transverse spin density of spatially confined light, Phys. Rev. X **8**, 021042 (2018).
[43] M. Benelajla, E. Kammann, B. Urbaszek, and K. Karrai, Physical origins of extreme cross-polarization extinction in confocal microscopy, Phys. Rev. X **11**, 021007 (2021).
[44] A. Ciattoni, G. Cincotti, and C. Palma, Angular momentum dynamics of a paraxial beam in a uniaxial crystal, Phys. Rev. E **67**, 036618 (2003).
[45] S. Fu, C. Guo, G. Liu, Y. Li, H. Yin, Z. Li, and Z. Chen, Spin-orbit optical Hall effect, Phys. Rev. Lett. **123**, 243904 (2019).
[46] W. Zhu, H. Zheng, Y. Zhong, J. Yu, and Z. Chen, Wave-vector-varying Pancharatnam-Berry phase photonic spin Hall effect, Phys. Rev. Lett. **126**, 083901 (2021).
[47] X. Chen, S. Wang, C. You, O. S. Magaña Loaiza, and R.-B. Jin, Experimental implementation of the fractional-vortex Hilbert hotel, Phys. Rev. A **106**, 033521 (2022).
[48] J. Wang, L. Shi, and J. Zi, Spin Hall effect of light via momentum-space topological vortices around bound states in the continuum, Phys. Rev. Lett. **129**, 236101 (2022).
[49] M. V. Berry, Interpreting the anholonomy of coiled light, Nature **326**, 277 (1987).
[50] K. Y. Bliokh, Y. Gorodetski, V. Kleiner, and E. Hasman, Coriolis effect in optics: Unified geometric phase and spin-Hall effect, Phys. Rev. Lett. **101**, 030404 (2008).
[51] X. Ling, X. Zhou, K. Huang, Y. Liu, C.-W. Qiu, H. Luo, and S. Wen, Recent advances in the spin Hall effect of light, Rep. Prog. Phys. **80**, 066401 (2017).
[52] T. Zhu, Y. Lou, Y. Zhou, J. Zhang, J. Huang, Y. Li, H. Luo, S. Wen, S. Zhu, Q. Gong, M. Qiu, and Z. Ruan, Generalized spatial differentiation from the spin Hall effect of light and its application in image processing of edge detection, Phys. Rev. Appl. **11**, 034043 (2019).
[53] S. He, J. Zhou, S. Chen, W. Shu, H. Luo, and S. Wen, Wavelength-independent optical fully differential operation based on the spin-orbit interaction of light, APL Photonics **5**, 036105 (2020).
[54] T. Zhu, J. Huang, and Z. Ruan, Optical phase mining by adjustable spatial differentiator, Adv. Photonics **2**, 016001 (2020).
[55] R. Wang, S. He, and H. Luo, Photonic spin-Hall differential microscopy, Phys. Rev. Appl. **18**, 044016 (2022).
[56] T. Zhu, Y. Zhou, Y. Lou, H. Ye, M. Qiu, Z. Ruan, and S. Fan, Plasmonic computing of spatial differentiation, Nat. Commun. **8**, 15391 (2017).
[57] J. Zhou, H. Qian, C. F. Chen, J. Zhao, G. Li, Q. Wu, H. Luo, S. Wen, and Z. Liu, Optical edge detection based on high-efficiency dielectric metasurface, Proc. Natl. Acad. Sci. USA **116**, 11137 (2019).
[58] Y. Zhou, H. Y. Zheng, I. I. Kravchenko, and J. Valentine, Flat optics for image differentiation, Nat. Photonics **14**, 316 (2020).

[59] Z. Wang, G. Hu, X. Wang, X. Ding, K. Zhang, H. Li, S. N. Burokur, Q. Wu, J. Liu, J. Tan, and C. W. Qiu, Single-layer spatial analog meta-processor for imaging processing, Nat. Commun. **13**, 1 (2022).

[60] H. Kwon, D. Sounas, A. Cordaro, A. Polman, and A. Alù, Nonlocal metasurfaces for optical signal processing, Phys. Rev. Lett. **121**, 173004 (2018).

[61] W. Southwell, Wave-front estimation from wave-front slope measurements, J. Opt. Soc. Am. **70**, 998 (1980).

[62] C. A. Casacio, L. S. Madsen, A. Terrasson, M. Waleed, K. Barnscheidt, B. Hage, M. A. Taylor, and W. P. Bowen, Quantum-enhanced nonlinear microscopy, Nature **594**, 201 (2021).

[63] J. Liu, Q. Yang, S. Chen, Z. Xiao, S. Wen, and H. Luo, Intrinsic optical spatial differentiation enabled quantum dark-field microscopy, Phys. Rev. Lett. **128**, 193601 (2022).

[64] P. Chen, C. Shu, X. Guo, M. M. T. Loy, and S. Du, Measuring the biphoton temporal wave function with polarization-dependent and time-resolved two-photon interference, Phys. Rev. Lett. **114**, 010401 (2015).

[65] A. O. C. Davis, V. Thiel, M. Karpinski, and B. J. Smith, Measuring the single-photon temporal-spectral wave function, Phys. Rev. Lett. **121**, 083602 (2018).

[66] S. Zhang, Y. Zhou, Y. Mei, K. Liao, Y. L. Wen, J. Li, X. D. Zhang, S. Du, H. Yan, and S. L. Zhu, δ-quench measurement of a pure quantum-state wave function, Phys. Rev. Lett. **123**, 190402 (2019).

[67] N. K. Berger, B. Levit, B. Fischer, M. Kulishov, D. V. Plant, and J. Azana, Temporal differentiation of optical signals using a phase-shifted fiber Bragg grating, Opt. Express **15**, 371 (2007).

[68] W. Liu, M. Li, R. S. Guzzon, E. J. Norberg, J. S. Parker, M. Lu, L. A. Coldren, and J. Yao, A fully reconfigurable photonic integrated signal processor, Nat. Photonics **10**, 190 (2016).

[69] J. Sol, D. R. Smith, and P. del Hougne, Meta-programmable analog differentiator, Nat. Commun. **13**, 1 (2022).

[70] Y. Qin, Y. Li, X. Feng, Y.-F. Xiao, H. Yang, and Q. Gong, Observation of the in-plane spin separation of light, Opt. Express **19**, 9636 (2011).